INTERNATIONAL JOURNAL FOR NUMERICAL METHODS IN FLUIDS
Int. J. Numer. Meth. Fluids 2009; **60**:1259–1288
Published online 17 November 2008 in Wiley InterScience (www.interscience.wiley.com). DOI: 10.1002/fld.1934

Quantitative benchmark computations of two-dimensional bubble dynamics

S. Hysing[1,*,†], S. Turek[2], D. Kuzmin[2], N. Parolini[3], E. Burman[4], S. Ganesan[5] and L. Tobiska[6]

[1]*Universitat Politècnica de Catalunya (UPC), Jordi Girona 1-3, Edifici C1, 08034 Barcelona, Spain*
[2]*Institut für Angewandte Mathematik, TU Dortmund, Vogelpothsweg 87, 44227 Dortmund, Germany*
[3]*MOX, Dipartimento di Matematica, Politecnico di Milano, Via Bonardi 29, 20133 Milano, Italy*
[4]*Department of Mathematics, University of Sussex, Brighton BN1 9RF, U.K.*
[5]*Department of Aeronautics, Imperial College, London, U.K.*
[6]*Institut für Analysis und Numerik, Otto-von-Guericke Universität, 39016 Magdeburg, Germany*

SUMMARY

Benchmark configurations for *quantitative* validation and comparison of incompressible interfacial flow codes, which model two-dimensional bubbles rising in liquid columns, are proposed. The benchmark quantities: circularity, center of mass, and mean rise velocity are defined and measured to monitor convergence toward a reference solution. Comprehensive studies are undertaken by three independent research groups, two representing Eulerian level set finite-element codes and one representing an arbitrary Lagrangian–Eulerian moving grid approach.

The first benchmark test case considers a bubble with small density and viscosity ratios, which undergoes moderate shape deformation. The results from all codes agree very well allowing for target reference values to be established. For the second test case, a bubble with a very low density compared to that of the surrounding fluid, the results for all groups are in good agreement up to the point of break up, after which all three codes predict different bubble shapes. This highlights the need for the research community to invest more effort in obtaining reference solutions to problems involving break up and coalescence.

Other research groups are encouraged to participate in these benchmarks by contacting the authors and submitting their own data. The reference data for the computed benchmark quantities can also be supplied for validation purposes. Copyright © 2008 John Wiley & Sons, Ltd.

Received 12 February 2008; Revised 15 July 2008; Accepted 21 August 2008

*Correspondence to: S. Hysing, Universitat Politècnica de Catalunya (UPC), Jordi Girona 1-3, Edifici C1, 08034 Barcelona, Spain.
†E-mail: shuren@cimne.upc.edu, shuren.hysing@math.uni-dortmund.de

Contract/grant sponsor: German Research foundation (DFG); contract/grant number: To143/9
Contract/grant sponsor: Paketantrag PAK178; contract/grant numbers: Tu102/27-1, Ku1530/5-1
Contract/grant sponsor: Sonderforschungsbereich SFB708; contract/grant number: TP B7
Contract/grant sponsor: SFB TR R30; contract/grant number: TPC3
Contract/grant sponsor: Swiss National Science Foundation; contract/grant number: 112166

KEY WORDS: benchmarking; multiphase flow; rising bubble; numerical simulation; finite-element method; level set method; ALE

1. INTRODUCTION

Numerical simulation of incompressible interfacial flows, such as two-phase flows with immiscible fluids, is maturing at a rapid rate. Numerous improved schemes and methods for numerically simulating mixtures of immiscible fluids undergoing complex topological changes are published every year (see, for example, References [1–11]), and thus it is perhaps somewhat surprising that no rigorous, that is *quantitative*, numerical benchmark configuration has been proposed for validation and comparison of interfacial flow codes to this date. This is in stark contrast to other fields of computational fluid dynamics (CFD) for which dedicated benchmarks have been presented and accepted by the CFD community [12–17].

The most common approach to validate interfacial flow codes is to examine the 'picture norm'. This means to qualitatively compare the computed interface shapes with reference solutions from simplified analytical expressions, numerical simulations, and experimental studies such as the bubble-shape diagrams established by Clift *et al.* [18] and Bhaga and Weber [19]. One frequently used test case for validation of two-phase flow codes is the classical dam break experiment by Martin and Moyce [20]. Although the dam break benchmark can be helpful for rough calibration in the early stages of code development, the limited accuracy in the experimental data and negligible influence of surface tension effects restricts its subsequent use. Prediction of real-life engineering problems may be the final goal of simulation software and numerical codes, but one should be careful not to limit the validation process to just comparing with experimental results. This is particularly true in the case of multiphase flow codes, which usually are very complex and often contain *ad hoc* modifications to produce a sought physical behavior. The first step should be to ascertain that the posed problem and governing equations are solved accurately, only then can one proceed to judge whether the mathematical model describes the physical reality well enough. If this has not been established, one simply cannot be sure that agreement with experiments is not partly due to specific tuning of the code, implementational aspects, or a fortunate coincidence, all of which could undermine the capability of the software to produce accurate solutions for a general class of problems.

In the absence of analytical solutions, which are very hard to come by for the considered problem class, validation of the mathematical model is best accomplished with numerical benchmarking. Pure numerical benchmarks on the other hand are of limited use if they cannot be employed to make quantitative comparisons, mere visual inspection is rarely, if ever, enough to draw hard conclusions. To illustrate this, consider the bubble shapes shown in Figure 1. These shapes are calculated by six different codes with identical problem formulations. They should thus ideally give six identical solutions. Unfortunately this is not the case. The shapes are quite similar but it is not possible to tell which solutions, if any, are really correct. In order to be able to do this, one must leave the 'picture norm' behind and instead use some rigid metrics with which convergence can be measured directly.

With this in mind two benchmark configurations are proposed and rigorous benchmark quantities are defined to measure direct topological parameters, such as interface deformation, and also indirect ones, such as velocity. The task of the proposed benchmarks is to track the evolution of a two-dimensional bubble rising in a liquid column. This configuration is simple enough to

DOI: 10.1002/fld

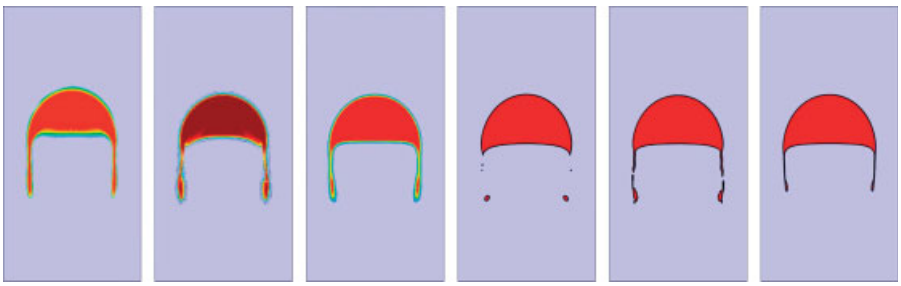

Figure 1. Numerical simulations of a two-dimensional rising bubble for six different codes with identical problem formulations.

compute accurately yet allows for very complex topology change, giving the interface capturing techniques of today an adequate challenge. The final goal of the numerical benchmarks is not to provide comparisons with experimental configurations, but to establish reference solutions for the benchmark quantities. These can then be used to rigorously determine if a given code solves the posed problem correctly and also greatly assist when comparing the efficiency of different methodologies to each other.

The outline of the paper is as follows. Section 2 introduces the governing equations and defines the two test cases. This is followed by descriptions of the algorithms and codes used by the participating groups in the computational benchmark studies (Section 3). The results for the two test cases computed by these groups are presented and compared in Sections 4 and 5. The paper is concluded, in Section 6, by summarizing the benchmark studies and briefly discussing their implications on future research.

2. DEFINITION OF TEST CASES

This section describes the governing equations, and defines the test cases and benchmark quantities to be used for validation of interfacial flow codes.

2.1. Governing equations

The benchmarks consider isothermal, incompressible flows of immiscible fluids. The conservation of momentum and mass is described by the Navier–Stokes equations

$$\rho(\mathbf{x})\left(\frac{\partial \mathbf{u}}{\partial t}+(\mathbf{u}\cdot\nabla)\mathbf{u}\right)=-\nabla p+\nabla\cdot(\mu(\mathbf{x})(\nabla\mathbf{u}+(\nabla\mathbf{u})^{\mathrm{T}}))+\rho(\mathbf{x})\mathbf{g}$$

$$\nabla\cdot\mathbf{u}=0$$

in a fixed space–time domain $\Omega\times[0,T]$, where $\Omega\subset\mathbb{R}^2$. These benchmarks are initially restricted to two dimensions since both computational complexity and time are greatly reduced. Here, $\rho(\cdot)$ and $\mu(\cdot)$ denote the density and viscosity of the fluids, $\mathbf{u}$ the velocity, p the pressure, and $\mathbf{g}$ the external gravitational force field. It is assumed that fluid 1 occupies the domain Ω_1 and that it

DOI: 10.1002/fld

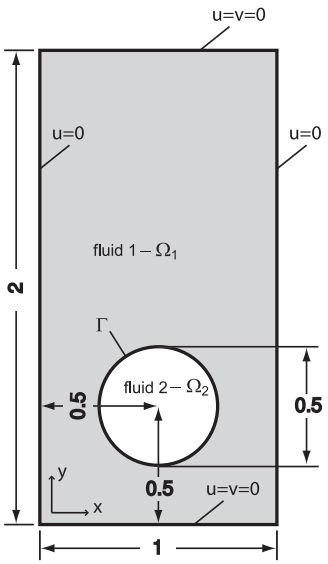

Figure 2. Initial configuration and boundary conditions for the test cases.

completely surrounds fluid 2 in Ω_2 (see Figure 2), in particular $\Gamma := \partial\Omega_1 \cap \partial\Omega_2$, $\Omega = \Omega_1 \cup \Gamma \cup \Omega_2$, and $\partial\Omega_2 \cap \partial\Omega = \emptyset$.

Surface tension effects are taken into consideration through the following force balance at the interface Γ:

$$[\mathbf{u}]|_\Gamma = 0, \quad [-p\mathbf{I} + \mu(\nabla\mathbf{u} + (\nabla\mathbf{u})^{\mathrm{T}})]|_\Gamma \cdot \hat{\mathbf{n}} = \sigma\kappa\hat{\mathbf{n}}$$

where $\hat{\mathbf{n}}$ is the unit normal at the interface pointing into Ω_1, $[\mathsf{A}]|_\Gamma = \mathsf{A}|_{\Omega_1\cap\Gamma} - \mathsf{A}|_{\Omega_2\cap\Gamma}$ denotes the jump of a quantity A across the interface, σ is the surface tension coefficient, and κ is the curvature of the interface Γ. The first condition implies continuity of the velocity across the interface, whereas the second describes the force balance on Γ. Two strategies are often used to handle the surface tension term, either to rewrite it as a volume force

$$\mathbf{f}_{st} = \sigma\kappa\hat{\mathbf{n}}\delta(\Gamma, \mathbf{x})$$

where $\delta(\Gamma, \mathbf{x})$ is the Dirac delta function localizing the surface tension forces to the interface, or to introduce the Laplace–Beltrami operator applied to the identity $\mathrm{id}: \mathbb{R}^2 \to \mathbb{R}^2$

$$\kappa\hat{\mathbf{n}} = \Delta_\Gamma \mathrm{id}$$

and integrating the corresponding term in the weak formulation of the problem by parts [21, 22].

2.2. *Initial configuration*

The initial configuration, see Figure 2, is identical for both test cases and consists of a circular bubble of radius $r_0 = 0.25$ centered at $[0.5, 0.5]$ in a $[1 \times 2]$ rectangular domain. The density of the bubble is smaller than that of the surrounding fluid ($\rho_2 < \rho_1$). The no-slip boundary condition ($\mathbf{u} = 0$) is used

DOI: 10.1002/fld

at the top and bottom boundaries, whereas the free slip condition ($\mathbf{u}\cdot\hat{\mathbf{n}}=0$, $\hat{\boldsymbol{\tau}}\cdot(\nabla\mathbf{u}+(\nabla\mathbf{u})^{\mathrm{T}})\cdot\hat{\mathbf{n}}=0$, $\hat{\boldsymbol{\tau}}$—the tangent vector) is imposed on the vertical walls.

2.3. Test case classification

Non-dimensionalization is frequently used to assist with classifying simulations and can be introduced by scaling the length with a given characteristic length scale, in this case $L=2r_0$, and the time with L/U_g where $U_g=\sqrt{g2r_0}$ is the gravitational velocity. The Reynolds number describing the ratio of inertial to viscous effects and the Eötvös number which gives the ratio of gravitational forces to surface tension effects can then be defined as

$$Re=\frac{\rho_1 U_g L}{\mu_1}, \quad Eo=\frac{\rho_1 U_g^2 L}{\sigma}$$

Here, the subscript 1 refers to the surrounding heavier fluid and the subscript 2 to the lighter fluid of the bubble. Moreover, r_0 is the initial radius of the bubble and g is the gravitational constant. The density ratio ρ_1/ρ_2 and viscosity ratio μ_1/μ_2 finally help to fully classify the test cases.

2.4. The test cases

Table I lists the fluid and physical parameters which specify the test cases. The evolution of the bubbles should be tracked for 3 time units during which the defined benchmark quantities should be measured. The first test case models a rising bubble with $Re=35$, $Eo=10$, and both density and viscosity ratios equal to 10. According to the experimental studies by Clift *et al.* [18], such a bubble will end up in the ellipsoidal regime. Assuming that this also is true for a two-dimensional bubble, it would mean that the surface tension effects are strong enough to hold the bubble together and thus one should not expect break up to occur in this test case.

The second and more challenging test case models a rising bubble with $Re=35$, $Eo=125$, and large density and viscosity ratios (1000 and 100). This bubble lies somewhere between the skirted and dimpled ellipsoidal-cap regimes indicating that break up can possibly occur [18], which will present additional challenges to the different interface tracking algorithms.

2.5. Benchmark quantities

Visual comparison of the results, and in particular visualization of the bubble interface, is one obvious way to compare simulations. However, this does not allow one to rigorously determine how accurate the simulations really are and, perhaps more interestingly, *how much numerical effort is required to attain a certain accuracy*? The following benchmark quantities, which will be used to assist in describing the temporal evolution of the bubbles quantitatively, are therefore introduced.

Table I. Physical parameters and dimensionless numbers defining the test cases.

Test case	ρ_1	ρ_2	μ_1	μ_2	g	σ	Re	Eo	ρ_1/ρ_2	μ_1/μ_2
1	1000	100	10	1	0.98	24.5	35	10	10	10
2	1000	1	10	0.1	0.98	1.96	35	125	1000	100

DOI: 10.1002/fld

Point quantities: Positions of various points can be used to track the translation of bubbles. It is common to use the centroid or center of mass (as used in References [5, 23–25]), defined by

$$\mathbf{X}_c = (x_c, y_c) = \frac{\int_{\Omega_2} \mathbf{x}\,\mathrm{d}x}{\int_{\Omega_2} 1\,\mathrm{d}x}$$

where Ω_2 denotes the region that the bubble occupies. Other points could be the absolute top or bottom of a bubble [5].

Circularity: The 'degree of circularity', introduced by Wadell [26], can in $\mathbb{R}^2$ be defined as

$$\phi = \frac{P_a}{P_b} = \frac{\text{perimeter of area-equivalent circle}}{\text{perimeter of bubble}} = \frac{\pi d_a}{P_b}$$

Here, P_a denotes the perimeter or circumference of a circle with diameter d_a, which has an area equal to that of a bubble with perimeter P_b. For a perfectly circular bubble or drop, the circularity will be equal to unity and decrease as the bubble is deformed.

Rise velocity: The mean velocity with which a bubble is rising or moving is a particularly interesting quantity since it does not only measure how the interface tracking algorithm behaves but also the quality of the overall solution. The mean bubble velocity is defined as

$$\mathbf{U}_c = \frac{\int_{\Omega_2} \mathbf{u}\,\mathrm{d}x}{\int_{\Omega_2} 1\,\mathrm{d}x}$$

where Ω_2 again denotes the region that the bubble occupies. A variant of this is simply to use the velocity at the centroid of the bubble $\mathbf{u}(\mathbf{X}_c)$. The velocity component in the direction opposite to the gravitational vector is usually denoted as rise velocity V_c, for which the stationary limit is called terminal velocity. Both rise and terminal velocities are, for example, used in References [23, 27].

2.6. Error quantification

The temporal evolution of the computed benchmark quantities can be measured against suitable reference solutions to establish the following relative error norms:

$$l_1 \text{ error:} \quad \|e\|_1 = \frac{\sum_{t=1}^{\mathrm{NTS}} |q_{t,\mathrm{ref}} - q_t|}{\sum_{t=1}^{\mathrm{NTS}} |q_{t,\mathrm{ref}}|}$$

$$l_2 \text{ error:} \quad \|e\|_2 = \left(\frac{\sum_{t=1}^{\mathrm{NTS}} |q_{t,\mathrm{ref}} - q_t|^2}{\sum_{t=1}^{\mathrm{NTS}} |q_{t,\mathrm{ref}}|^2} \right)^{1/2}$$

$$l_\infty \text{ error:} \quad \|e\|_\infty = \frac{\max_t |q_{t,\mathrm{ref}} - q_t|}{\max_t |q_{t,\mathrm{ref}}|}$$

where q_t is the temporal evolution of quantity q.

The solution computed on the finest grid with the smallest time step is usually taken as a reference solution $q_{t,\mathrm{ref}}$. Interpolation should be appropriately applied if there are more time steps or sample points (NTS) for the reference solution than the solutions q_t for which the error norms should be computed. Standard linear interpolation was used throughout the conducted studies to account for this difference in the temporal sample rates.

DOI: 10.1002/fld

With the relative errors established and CPU times measured, it is then straightforward to see how much effort is required to establish a certain accuracy. Additionally, convergence rates (ROC) for the quantities can also be computed as

$$\mathrm{ROC} = \frac{\log_{10}(\|e^{l-1}\|/\|e^{l}\|)}{\log_{10}(h^{l-1}/h^{l})}$$

where l is the grid refinement level and h the mean cell edge length.

In the following studies, the finest grid solution of each respective group is taken as their own reference solution. The ROC will, therefore, not indicate how well a method converges to the exact solution, but how it converges toward an approximate discrete solution. Although this means that absolute convergence cannot be proved, if the results from a sufficient number of methods and groups approach the same solution it can be assumed that the difference between the discrete reference solutions and the exact solution is not too large.

3. PARTICIPATING GROUPS

Computational studies of the proposed benchmarks were performed by the groups listed in Table II. Their corresponding methods and codes are described in the following.

3.1. Group 1: TP2D

The TP2D code (short for **T**ransport **P**henomena in **2D**) is an extension of the Featflow incompressible flow solver to treat immiscible fluids with the level set method [28, 29].

TP2D is based on finite-element discretizations in space with non-conforming $\widetilde{\mathbb{Q}}_1\mathbb{Q}_0$ basis functions for the flow variables and a conforming $\mathbb{Q}_1$ bilinear approximation for the level set function. Time discretization of the governing equations is optionally done with either second-order one- or fractional-step-theta schemes. The velocity and pressure flow variables are decoupled from each other with the discrete projection method, which, in conjunction with a geometrical multigrid approach to solve the involved linear systems, has proved to be a very efficient way to solve time-dependent problems [29]. In each time step the dependent variables are thus treated sequentially (momentum equations, pressure Poisson equation, and the level set equation).

In order to keep the level set function from deviating too much from a distance function, one can periodically apply some form of reinitialization. There are a number of options available in the TP2D code, of which the most efficient is a combination of the fast marching method for the far field and direct initialization of the interface nodes [30]. A mass correction step can also be applied

Table II. Participating groups and methods.

	Group and affiliation	Code/method
1	TU Dortmund, Inst. of Applied Math.	**TP2D**
	S. Turek, D. Kuzmin, S. Hysing	*FEM-Level Set*
2	EPFL Lausanne, Inst. of Analysis and Sci. Comp.	**FreeLIFE**
	E. Burman, N. Parolini	*FEM-Level Set*
3	Uni. Magdeburg, Inst. of Analysis and Num. Math.	**MooNMD**
	L. Tobiska, S. Ganesan	*FEM-ALE*

DOI: 10.1002/fld

to the level set function by addition of a suitable constant and thus globally lowering/raising it by a small amount. This only introduces a small change to the level set field, which may be necessary to prevent accumulation of mass errors for time-dependent simulations.

The low *Re* numbers of the proposed benchmarks did not necessitate the use of artificial stabilization for the convective terms in the momentum equations. Artificial stabilization was only used with the level set equation and then in the form of high-order FEM-TVD [31]. Surface tension effects were incorporated by straight line approximation of the interface contours and direct integration over these line segments instead of using the usual continuum surface force approach. More details on the implementation, solver aspects, and surface tension treatment can be found in References [29, 32–34].

3.2. Group 2: FreeLIFE

The FreeLIFE (**Free**-Surface **Li**brary of **F**inite **E**lement) software is an incompressible flow solver for the solution of free-surface two-fluid problems. The software is based on the numerical solution of the Navier–Stokes equations with variable density and viscosity. In order to track the location of the interface between the two fluids, where discontinuities in the density and viscosity occur, a level set approach is adopted. The Navier–Stokes equations are, therefore, coupled with an advection equation for the level set function whose zero level set defines the interface location [35, 36].

The spatial discretization is based on a piecewise linear finite-element approach. In particular, the Navier–Stokes problem is solved using $\mathbb{P}_1$-iso$\mathbb{P}_2$ elements for the velocity and $\mathbb{P}_1$ for the pressure. The sub-grid topology associated with the $\mathbb{P}_1$-iso$\mathbb{P}_2$ element is also exploited for the solution of the level set transport equation, where the local sub-grid edge stabilization introduced in [37] has been adopted. In the simulations presented here, to be consistent with the method of group 1, a mass correction step has been added, which consists in lowering/raising the level set function by a constant value in order to guarantee a global mass conservation.

The level set reinitialization is based on a new method proposed in [35] consisting of a local (L^2-projection-based) reconstruction of the distance function in the neighborhood of the interface and a fast marching strategy for the far field [38]. The time discretization is based on the second-order BDF2 scheme and an algebraic factorization technique is used for the solution of the Navier–Stokes system.

The FreeLIFE software has been used for the simulation of a variety of test cases concerning laminar two-fluid flows. The results of these simulations have been presented and discussed in [35, 36, 39]. The method has been implemented in a finite-element library, which is restricted to two-dimensional problems. However, the proposed methodology is well suited for the solution of three-dimensional problems. This approach is currently being extended to three-dimensional problems in the framework of the library *LifeV*, a three-dimensional finite-element code developed in a joint collaboration between Ecole Polytechnique Fédérale de Lausanne (CMCS), Politecnico di Milano (MOX), and INRIA (BANG).

3.3. Group 3: MooNMD

MooNMD stands for **M**athematics and **o**bject-**o**riented **N**umerics in **M**ag**D**eburg [40]. It is a program package based on mapped finite-element methods for discretizing partial differential equations. In particular, it covers the solution of the incompressible Navier–Stokes equations by inf–sup stable isoparametric finite elements [41] and the solution of convection–diffusion equations

DOI: 10.1002/fld

by stabilized finite-element methods. It has been extended to treat incompressible two-phase flows with capillary forces using the arbitrary Lagrangian–Eulerian approach.

For the benchmarks, the velocity components were discretized on simplex grids by quadratic basis functions enriched with cubic polynomial functions, and the pressure by discontinuous piecewise linear elements. In this way, high accuracy could be achieved and spurious velocities suppressed [42]. It is worth mentioning that no mass correction step was applied. Furthermore, the curvature in the surface tension term was replaced by the Laplace–Beltrami operator, which can be integrated by parts and thus reduce the smoothness requirements [21, 43, 44].

For the time discretization, the second order, strongly A-stable fractional-step-theta scheme was used [45]. In each time step the interface was fully resolved by the mesh, meaning that the interface was always aligned with cell edges. Three to four different initial meshes were generated using the mesh generator Triangle [46] by fixing 200–900 degrees of freedom on the interface. The movement of the interface was done in a Lagrangian manner after which the inner mesh points were fitted to the new interface by an elastic mesh update, that is by solving a linear elasticity problem [22]. It turned out that no remeshing, to improve the mesh quality, was needed for long periods. During such a period the number of degrees of freedom was fixed. However, remeshing had to be applied after some time depending on the degree of deformation, which changed the number of degrees of freedom dynamically during the simulations.

4. RESULTS FOR TEST CASE 1

In test case 1 the bubble, being initially circular, is stretched horizontally and first develops a dimple as it rises, but after some time proceeds to assume a more stable ellipsoidal shape.

4.1. Group 1: TP2D

The results for test case 1 computed with the TP2D code of group 1 are presented here. All computations were performed on rectangular tensor product grids with cell sizes $h = 1/[40, 80, 160, 320]$. The implicit second-order Crank–Nicolson scheme was used with the time step fixed to $\Delta t = h/16$. Table III shows the simulation statistics for the different grid levels where the number of elements is denoted by NEL, the total number of degrees of freedom by NDOF, and the total number of time steps by NTS. The time in seconds required for each computation is denoted by CPU. The Fortran 77 TP2D code was compiled with the PathScale v2.5 compiler suite and the computations were performed on servers with 2.4 GHz AMD Opteron processors.

In Figure 3 the coarse grid bubble shapes at the final time ($t = 3$) are compared with the solution from the computation on the finest grid ($h = \frac{1}{320}$). It is apparent that the solution on the coarsest grid $h = \frac{1}{40}$ (Figure 3(a)) is already quite good but does visibly differ somewhat from the reference

Table III. Simulation statistics and timings for test case 1 and group 1 (TP2D).

$1/h$	NEL	NDOF	NTS	CPU
40	3200	19561	1920	181
80	12800	77521	3840	1862
160	51200	308641	7680	20360
320	204800	1231681	15360	126373

DOI: 10.1002/fld

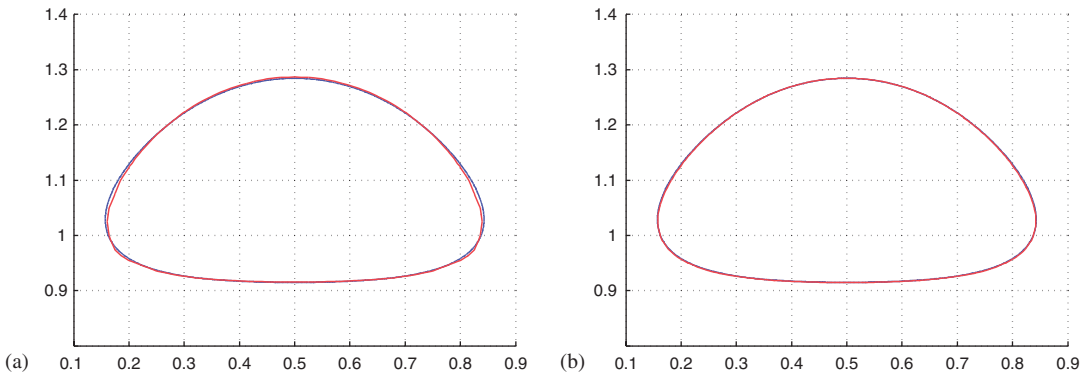

Figure 3. Test case 1 bubble shapes for the TP2D code at time $t=3$. Coarse grid solutions (shown in red) compared with the shape computed on the finest grid $h=\frac{1}{320}$ (shown in blue): (a) $h=\frac{1}{40}$ and (b) $h=\frac{1}{80}$.

Table IV. Relative error norms and convergence orders for test case 1 and group 1 (TP2D).

$1/h$	$\|e\|_1$	ROC_1	$\|e\|_2$	ROC_2	$\|e\|_\infty$	ROC_∞
Circularity						
40	1.00e−03		1.22e−03		2.89e−03	
80	3.01e−04	1.74	3.63e−04	1.75	9.67e−04	1.58
160	8.83e−05	1.77	1.10e−04	1.72	4.32e−04	1.16
Center of mass						
40	2.65e−03		2.99e−03		3.56e−03	
80	9.64e−04	1.46	1.02e−03	1.55	1.14e−03	1.64
160	2.62e−04	1.88	2.71e−04	1.91	2.96e−04	1.95
Rise velocity						
40	1.19e−02		1.29e−02		1.49e−02	
80	2.90e−03	2.04	3.07e−03	2.07	5.08e−03	1.55
160	7.73e−04	1.91	7.85e−04	1.97	1.94e−03	1.39

solution. The computation on an one level finer grid ($h=\frac{1}{80}$ shown in Figure 3(b)) shows closer agreement and further refinements yield bubble shapes that are visually indistinguishable from the reference shape. Merely looking at the bubble shapes is clearly not sufficient to say anything about the accuracy on the finer grids, and it is now that the previously defined benchmark quantities become particularly useful.

The relative error norms for the circularity, center of mass, and rise velocity are shown in Table IV together with the estimated ROC. The reference solution remains the one from the computation on the finest grid ($h=\frac{1}{320}$). It is evident that all quantities converge with a more than linear convergence order, approaching quadratic convergence in the l_1 and l_2 norms. In the maximum norm, the convergence order decreased to 1.16 for the circularity and 1.39 for the rise velocity.

The following figures depict the time evolution of the benchmark quantities for test case 1 and group 1 (TP2D). From Figure 4(a), which shows the circularity, it is quite hard to discern any significant differences between the different grids. Only for the coarsest grid ($h=\frac{1}{40}$) is it

DOI: 10.1002/fld

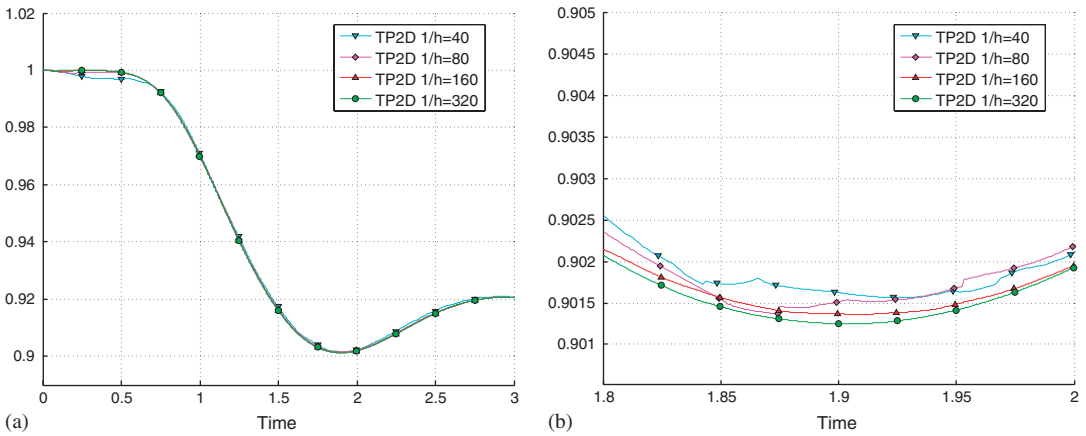

Figure 4. Circularity for test case 1 and group 1 (TP2D): (a) circularity and (b) close-up of the circularity.

Table V. Minimum circularity and maximum rise velocity, with corresponding incidence times, and the final position of the center of mass for test case 1 and group 1 (TP2D).

$1/h$	40	80	160	320
$\phi_{\min}$	0.9016	0.9014	0.9014	0.9013
$t\|_{\phi=\phi_{\min}}$	1.9234	1.8734	1.9070	1.9041
$V_{c,\max}$	0.2418	0.2418	0.2419	0.2417
$t\|_{V_c=V_{c,\max}}$	0.9141	0.9375	0.9281	0.9213
$y_c(t=3)$	1.0818	1.0810	1.0812	1.0813

possible to see some deviations; the circularity drops too quickly until $t=0.7$, after which the correct solution behavior is recovered. A close up around the point of minimum circularity is shown in Figure 4(b) from where it is possible to see the convergence behavior. Most notable is that there are irregularities or small jumps in the curves for the two coarsest grids, which is due to the reinitialization procedure that was applied every 20 time steps. The minimum circularity converges toward a value of 0.9013 around $t=1.90$ (see Table V).

Both the center of mass, shown in Figure 5(a), and the mean rise velocity of the bubble, shown in Figure 5(b), converge very nicely. From Table V, one can see that the maximum rise velocity of $V_{c,\max}=0.2417$ is attained quite early at time $t=0.92$. The center of mass of the bubble can asymptotically be described as a linear function of time and approaches $y_c=1.0813$ toward the end of the simulation.

4.2. *Group 2: FreeLIFE*

The following results are computed with the FreeLIFE code of the second group. The computations were performed on simplex cells created by subdivision of regular quadrilaterals with element mesh sizes $h=1/[40, 80, 160]$. The time step was chosen as $\Delta t=h/2$. Statistics and timings for the computations can be seen in Table VI. The FreeLIFE code was compiled with the Intel Fortran compiler and the simulations were performed on a workstation with a Pentium Xeon (2.8 GHz) processor.

DOI: 10.1002/fld

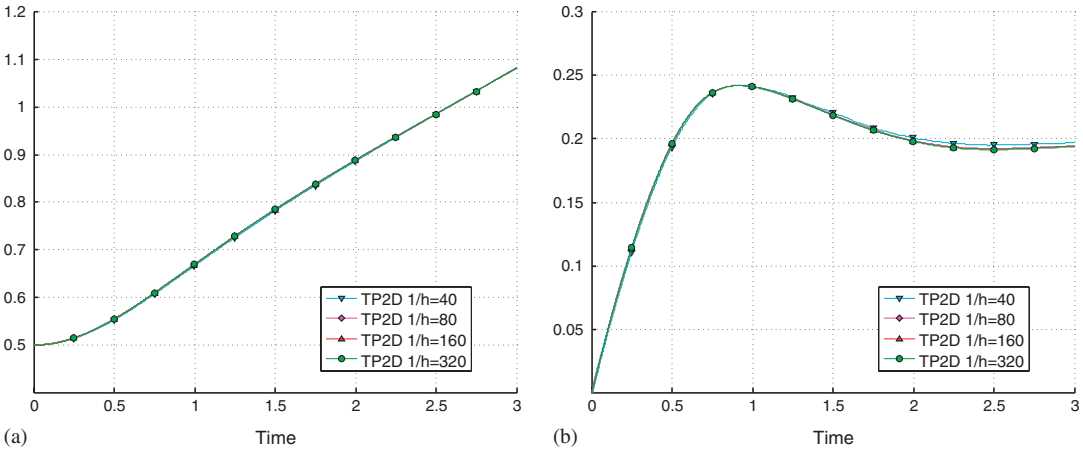

Figure 5. Center of mass and rise velocity for test case 1 and group 1 (TP2D): (a) center of mass and (b) rise velocity.

Table VI. Simulation statistics and timings for test case 1 and group 2 (FreeLIFE).

$1/h$	NEL	NDOF	NTS	CPU
40	6400	14145	240	257
80	25600	55485	480	4299
160	102400	219765	960	108846

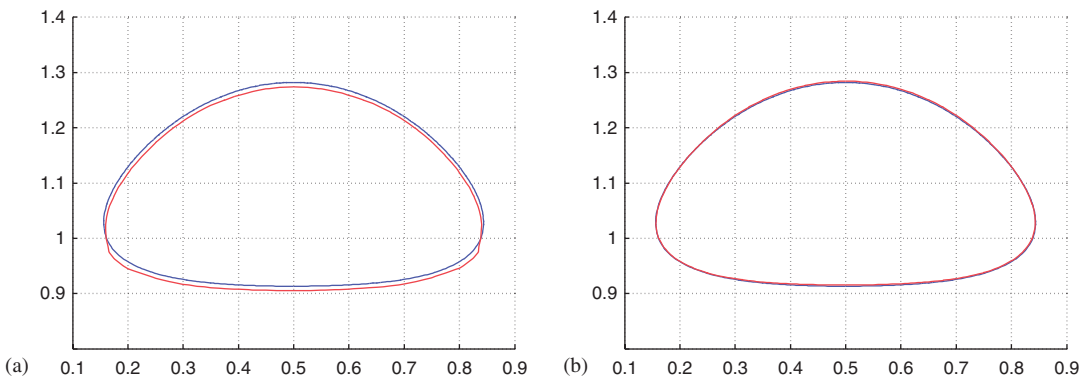

Figure 6. Test case 1 bubble shapes for the FreeLIFE code at time $t=3$. Coarse grid solutions (shown in red) compared with the shape computed on the finest grid $h=\frac{1}{160}$ (shown in blue): (a) $h=\frac{1}{40}$ and (b) $h=\frac{1}{80}$.

In Figure 6 the bubble shapes at the final time ($t=3$) with the different grid resolutions are compared. Although the interface contour from the solution on the coarsest grid seems to be offset in the y-direction, the overall shape is correct, and when the grid is refined once it is not anymore possible to distinguish between the two bubbles (Figure 6(b)).

DOI: 10.1002/fld

Table VII. Relative error norms and convergence orders for test case 1 and group 2 (FreeLIFE).

$1/h$	$\|e\|_1$	ROC_1	$\|e\|_2$	ROC_2	$\|e\|_\infty$	ROC_∞
Circularity						
40	2.61e−03		3.63e−03		8.09e−03	
80	1.05e−03	1.31	1.36e−03	1.41	2.51e−03	1.69
Center of mass						
40	7.85e−03		8.14e−03		7.74e−03	
80	9.42e−04	3.06	1.25e−03	2.70	1.72e−03	2.17
Rise velocity						
40	1.78e−02		1.95e−02		3.30e−02	
80	3.99e−03	2.16	5.54e−03	1.82	1.00e−02	1.72

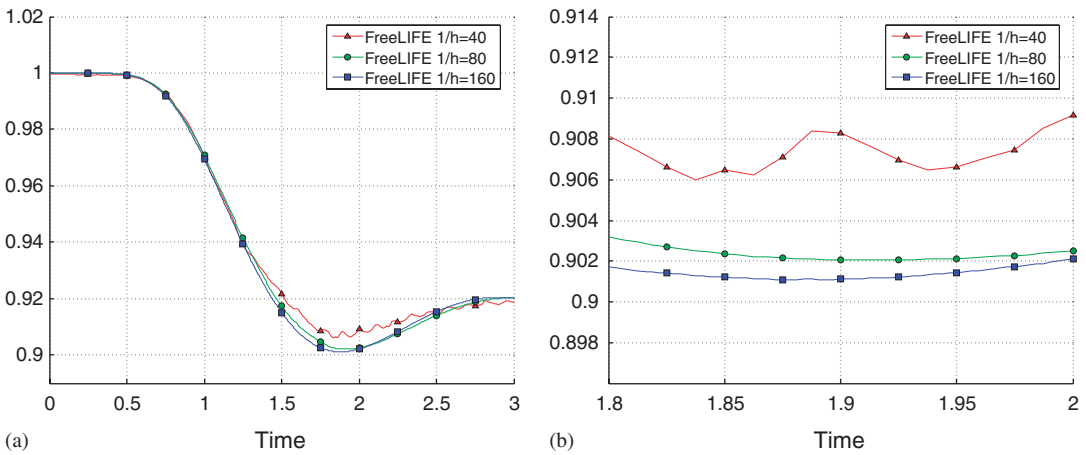

Figure 7. Circularity for test case 1 and group 2 (FreeLIFE): (a) circularity and (b) close-up of the circularity.

A quantitative convergence analysis has been performed computing the relative errors for the circularity, center of mass, and rise velocity together with the estimated ROC, as defined in Section 2.6. Here, the solution from the finest grid ($h=\frac{1}{160}$) is taken as the reference solution. As can be seen in Table VII, the method gives a convergence order approaching 1.5 for the circularity and about 2 for the rise velocity. The center of mass shows a very good convergence behavior of about 3 in the l_1 and l_2 norms and 2 in the l_∞ norm.

Figure 7 depicts the circularity for the three different grid levels. Although the solution on the coarsest grid is highly oscillating, the results converge toward the solution corresponding to the finest grid ($h=\frac{1}{160}$). The maximum deformation of the bubble is reached at time $t=1.88$ where the circularity attains its minimum value of 0.9011 (see Table VIII and Figure 7(b)).

The time evolutions of the center of mass and mean rise velocity can be seen in Figures 8(a) and (b), respectively. Both these quantities seem to converge, although the curve from the simulation on the coarsest grid deviates somewhat from the other two. The rise velocity reaches its maximum

DOI: 10.1002/fld

Table VIII. Minimum circularity and maximum rise velocity, with corresponding incidence times, and the final position of the center of mass for test case 1 and group 2 (FreeLIFE).

$1/h$	40	80	160
$\phi_{\min}$	0.9060	0.9021	0.9011
$t\|_{\phi=\phi_{\min}}$	1.8375	1.9125	1.8750
$V_{c,\max}$	0.2427	0.2410	0.2421
$t\|_{V_c=V_{c,\max}}$	0.9000	0.9375	0.9313
$y_c(t=3)$	1.0715	1.0817	1.0799

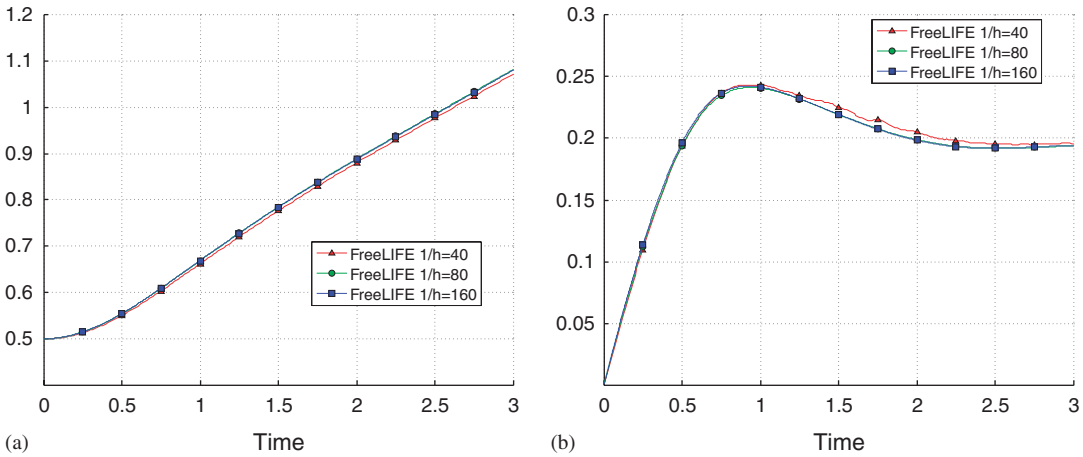

Figure 8. Center of mass and rise velocity for test case 1 and group 2 (FreeLIFE): (a) center of mass and (b) rise velocity.

Table IX. Simulation statistics and timings for test case 1 and group 3 (MooNMD).

NDOF_{int}	NEL $(t=0)$	NDOF	NTS	CPU
200	595	17 846	3000	11 034
300	2640	24 002	6000	25 110
600	5534	50 048	6000	58 349
900	8066	72 836	6000	180 819

value of 0.2421 at time $t=0.9313$ and center of mass of the bubble reaches a height of 1.08 at the end of the simulation (see Table VIII).

4.3. Group 3: MooNMD

Simulations of test case 1 with the MooNMD code of the third group were performed with 200, 300, 600, and 900 degrees of freedom resolving the interface (denoted by NDOF_{int}). The computations were run on a server with a 2.16 GHz Intel processor, for which simulation statistics are given in Table IX.

DOI: 10.1002/fld

Table X. Relative error norms and convergence orders for test case 1 and group 3 (MooNMD).

$NDOF_{int}$	$\|e\|_1$	ROC_1^*	$\|e\|_2$	ROC_2^*	$\|e\|_\infty$	ROC_∞^*
Circularity						
200	4.40e−04		5.99e−04		1.19e−03	
300	2.60e−04	1.30	3.40e−04	1.40	6.55e−04	1.47
600	1.07e−04	1.28	1.41e−04	1.27	2.90e−04	1.18
Center of mass						
200	5.07e−04		7.91e−04		1.53e−03	
300	1.79e−04	2.57	2.87e−04	2.50	5.82e−04	2.38
600	1.66e−05	3.43	2.11e−05	3.76	3.85e−05	3.92
Rise velocity						
200	2.87e−03		3.70e−03		5.96e−03	
300	1.18e−03	2.20	1.54e−03	2.17	2.48e−03	2.16
600	2.33e−04	2.34	3.10e−04	2.31	1.28e−03	0.95

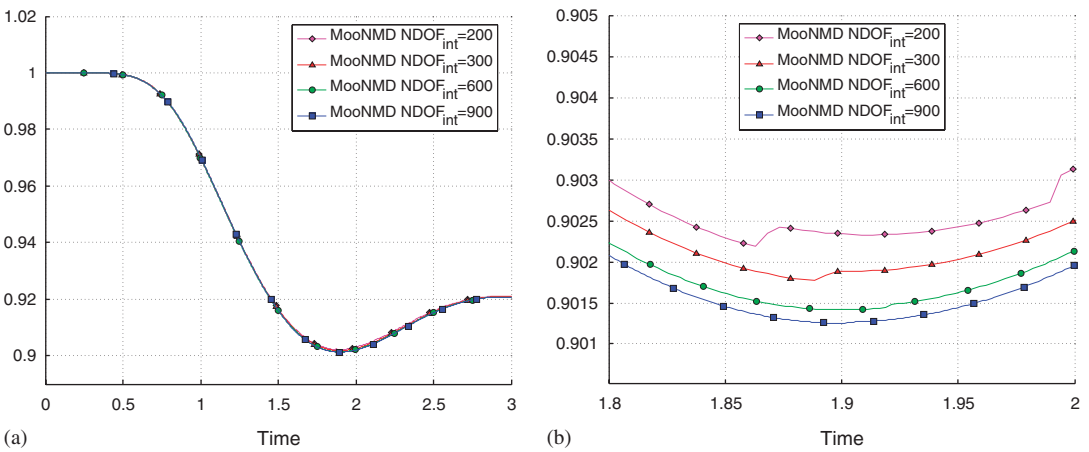

Figure 9. Circularity for test case 1 and group 3 (MooNMD): (a) circularity and (b) close-up of the circularity.

Table X shows the computed error norms and convergence orders for MooNMD. Since the finer meshes are not obtained by uniform refinement of the coarse mesh, but with the help of a mesh generator, h was replaced in the formula for calculating the ROC by h^*, the edge length of the interface at $t=0$. This is indicated in Table X by the notation ROC*. The center of mass and the rise velocity approach a convergence order of 3 and 2.2 in the l_1 and l_2 norms. In the l_∞ norm, the convergence order decreases for the rise velocity. The circularity had the overall lowest convergence order of 1.3.

That this method had very small error levels, even on the coarsest grids, is apparent from Figures 9(a) and 10, which depict the circularity, center of mass, and the rise velocity. There is no real visible evidence that any of the curves differ, even for the coarser grids, until one looks much closer (see Figure 9(b)). Then it is possible to see that each grid refinement produces results that are closer to the curve corresponding to the computation on the finest grid.

DOI: 10.1002/fld

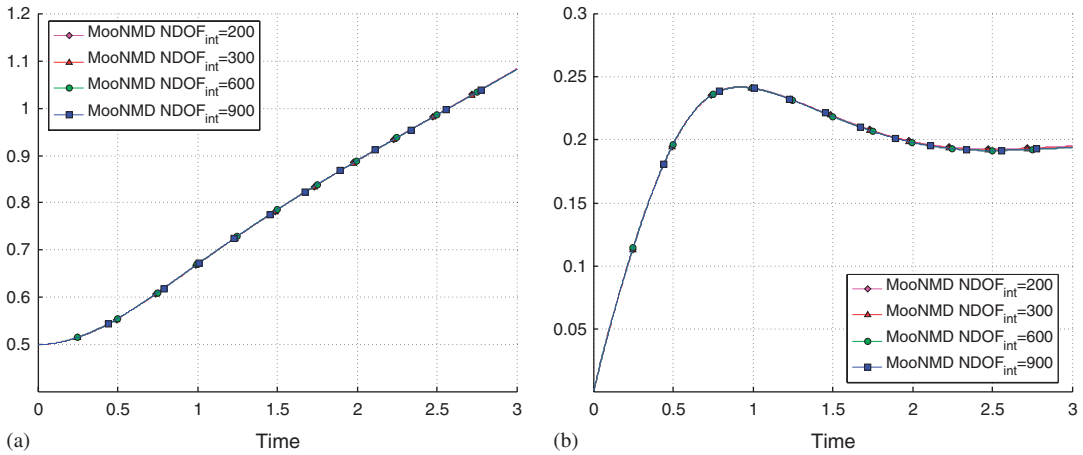

Figure 10. Center of mass and rise velocity for test case 1 and group 3 (MooNMD): (a) center of mass and (b) rise velocity.

Table XI. Minimum circularity and maximum rise velocity, with corresponding incidence times, and the final position of the center of mass for test case 1 and group 3 (MooNMD).

NDOF_{int}	200	300	600	900
$\phi_{\min}$	0.9022	0.9018	0.9014	0.9013
$t\|_{\phi=\phi_{\min}}$	1.8630	1.8883	1.9013	1.9000
$V_{c,\max}$	0.2418	0.2417	0.2417	0.2417
$t\|_{V_c=V_{c,\max}}$	0.9236	0.9236	0.9214	0.9239
$y_c(t=3)$	1.0833	1.0823	1.0818	1.0817

Table XI shows the time and values of the minimum circularity, maximum rise velocity, and maximum position of the center of mass achieved during the simulations. For the finest grid, a minimum circularity of 0.9013 was measured at time $t=1.9$. The rise velocity showed a very stable maximum, almost irrespective of the grid level, with a value of 0.2417 recorded at times around 0.92. At the final time the center of mass of the bubble had reached a position of 1.0817 on the finest grid.

4.4. Overall results for test case 1

Here, the results from all groups computations on the finest grids are compared starting with the bubble shapes shown in Figure 11. No significant differences can really be seen at all and one would thus expect the computed benchmark quantities to be similarly close.

The curves for the circularity shown in Figure 12(a) do not reveal any significant differences between the groups. Only in the enlarged section around the minimum (Figure 12(b)), is it possible to see some separation between the curves. The curves of groups 1 (TP2D) and 3 (MooNMD) agree best, while the minimum calculated by the second group (FreeLIFE) is somewhat offset. This is also reflected by the actual values shown in Table XII. From there it is possible to conclude that the minimum circularity will have a value of 0.9012 ± 0.0001 around $t=1.9$.

DOI: 10.1002/fld

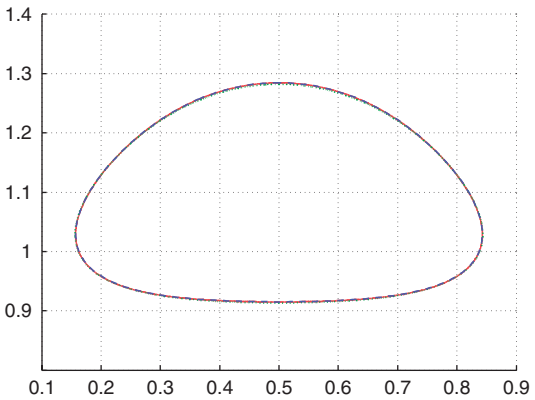

Figure 11. Bubble shapes at the final time ($t=3$) for test case 1 (TP2D (solid red), FreeLIFE (dotted green), and MooNMD (dashed blue)).

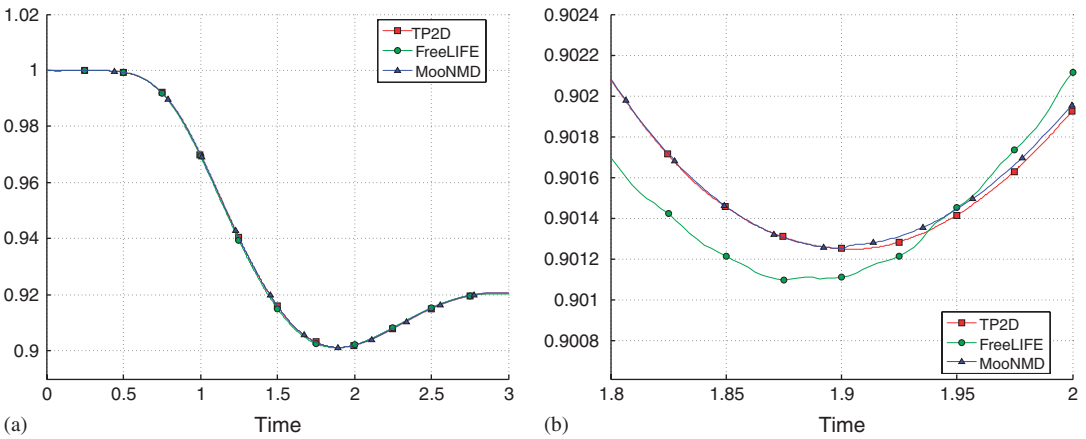

Figure 12. Circularity for test case 1 (all groups): (a) circularity and (b) close-up of the circularity.

Table XII. Minimum circularity and maximum rise velocity, with corresponding incidence times, and the final position of the center of mass for test case 1 (all groups).

Group	1	2	3
$\phi_{\min}$	0.9013	0.9011	0.9013
$t\|_{\phi=\phi_{\min}}$	1.9041	1.8750	1.9000
$V_{c,\max}$	0.2417	0.2421	0.2417
$t\|_{V_c=V_{c,\max}}$	0.9213	0.9313	0.9239
$y_c(t=3)$	1.0813	1.0799	1.0817

DOI: 10.1002/fld

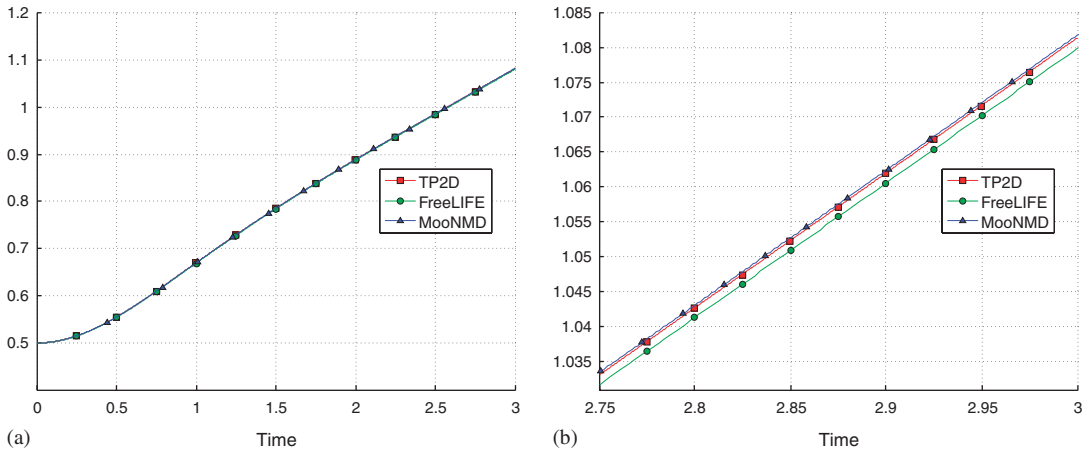

Figure 13. Center of mass for test case 1 (all groups): (a) center of mass and (b) close-up of the center of mass.

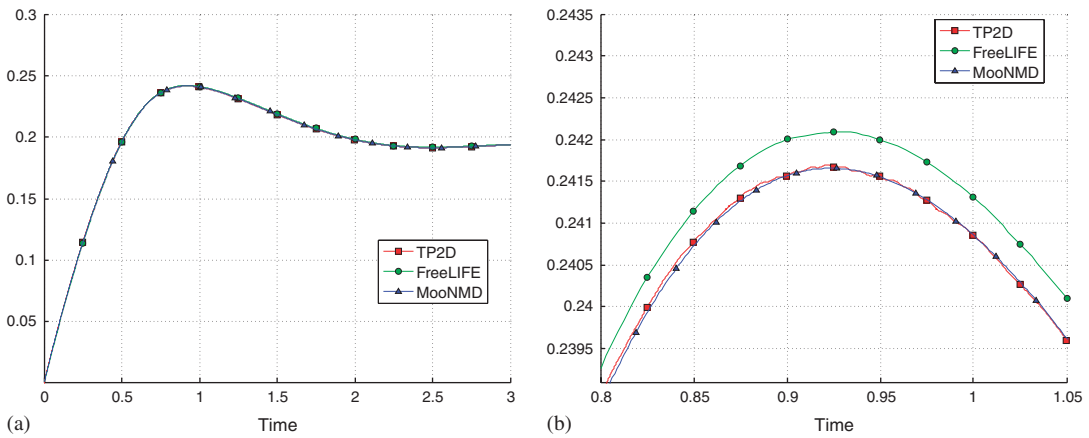

Figure 14. Rise velocity for test case 1 (all groups): (a) rise velocity and (b) close-up of the rise velocity.

The time evolution of the center of mass (Figure 13) essentially shows the same behavior as the circularity. The curves for groups 1 and 3 agree well, while the bubble of the second group seems to rise with the same speed but has been somewhat delayed (negative offset). From Table XII one can see that the center of mass of the bubble reaches a position of 1.081 ± 0.001 at the final time.

The last benchmark quantity to be examined for this test case is the mean rise velocity of the bubble, which is shown in Figure 14. Again the curves for groups 1 (TP2D) and 3 (MooNMD) agree very well while the curve for FreeLIFE (group 2) is slightly positively offset. The overall maximum rise velocity has a magnitude of 0.2419 ± 0.0002 and occurs between times $t = 0.921$ and 0.932.

DOI: 10.1002/fld

To summarize, computational studies of test case 1 have been conducted, which have made it possible to establish a target reference range for each of the benchmark quantities. However, the three different codes did not agree perfectly and one must conclude that numerical simulation of a single rising bubble, undergoing moderate deformation, is not even in two-dimensions a trivial task.

5. RESULTS FOR TEST CASE 2

Figure 15 shows snapshots of the time evolution of the bubble (computed by group 1 on a $h = \frac{1}{160}$ grid). Although the bubbles in both test cases rise with approximately the same speed, the decrease

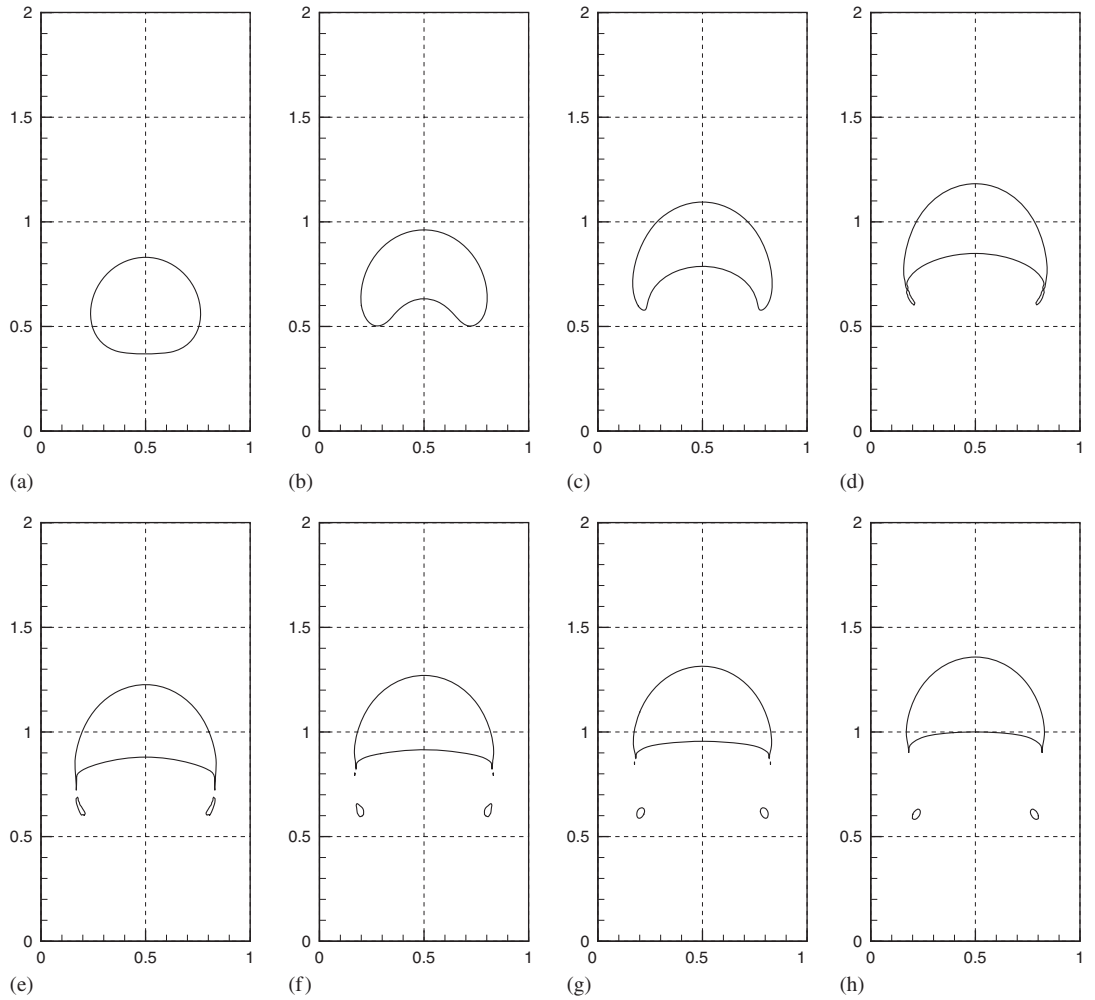

Figure 15. Typical time evolution of the interface for test case 2: (a) $t = 0.6$; (b) $t = 1.2$; (c) $t = 1.8$; (d) $t = 2.2$; (e) $t = 2.4$; (f) $t = 2.6$; (g) $t = 2.8$; and (h) $t = 3.0$.

DOI: 10.1002/fld

in surface tension causes this bubble to assume a more non-convex shape and develop thin filaments, which eventually break off. The time of break up is in this simulation predicted to occur between $t=2.2$ and 2.4, as is evident from Figures 15(d) and (e). After the break up, small satellite droplets trail the bulk of the main bubble, which eventually assumes the shape of a dimpled cap.

5.1. Group 1: TP2D

The bubble shapes at the final time ($t=3$), computed by the TP2D code of group 1, are shown in Figure 16. First of all one can see that the simulation on the coarsest grid produced a rather unphysical break up behavior, generating sharp-edged trailing filaments (Figure 16(a)). The shapes computed on the finer grids did not have these filaments and seemed to converge for the main bulk

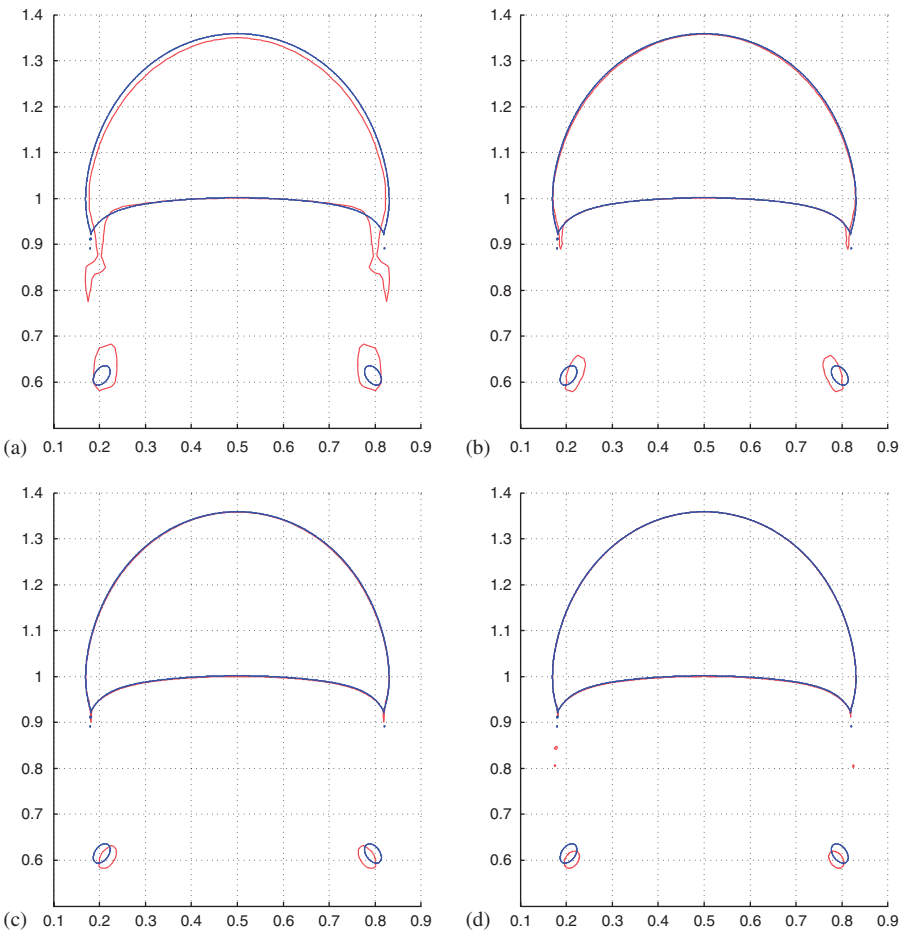

Figure 16. Test case 2 bubble shapes for the TP2D code at time $t=3$. Coarse grid solutions (shown in red) compared with the shape computed on the finest grid $h=\frac{1}{640}$ (shown in blue): (a) $h=\frac{1}{40}$; (b) $h=\frac{1}{80}$; (c) $h=\frac{1}{160}$; and (d) $h=\frac{1}{320}$.

DOI: 10.1002/fld

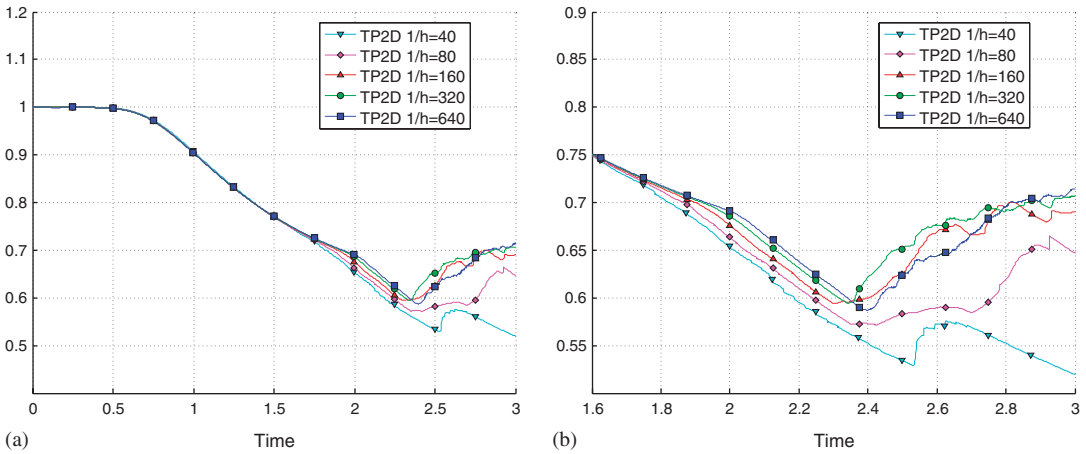

Figure 17. Circularity for test case 2 and group 1 (TP2D): (a) circularity and (b) close-up of the circularity.

Table XIII. Minimum circularity and maximum rise velocities, with corresponding incidence times, and the final position of the center of mass for test case 2 and group 1 (TP2D).

$1/h$	40	80	160	320	640
$\phi_{\min}$	0.5193	0.5717	0.5946	0.5943	0.5869
$t\|_{\phi=\phi_{\min}}$	3.0000	2.4266	2.2988	2.3439	2.4004
$V_{c,\max 1}$	0.2790	0.2638	0.2570	0.2538	0.2524
$t\|_{V_c=V_{c,\max 1}}$	0.7641	0.7250	0.7430	0.7340	0.7332
$V_{c,\max 2}$	0.2749	0.2597	0.2522	0.2467	0.2434
$t\|_{V_c=V_{c,\max 2}}$	1.9375	1.9688	2.0234	2.0553	2.0705
$y_c(t=3)$	1.1303	1.1370	1.1377	1.1387	1.1380

bubble. The small satellite droplets were apparently the most difficult to capture correctly since their shape and position even differed on the two finest grids (Figure 16(d)).

The circularity shown in Figure 17(a) is constant until $t=0.5$. It then decreases more or less linearly until somewhere between $t=2.2$ and 2.6 where there is a sharp inflection point (see Figure 17(b)). This point should be very close to the time of break up since the thin elongated filaments, due to the high curvature and surface tension, shrink quite rapidly thereafter. This is also consistent with Figures 15(d)–(f). The curves for all grid levels agree very well until $t=1.7$ where they start to deviate from each other. Although the deviations are also apparent from looking at the values of the minima in Table XIII, the numbers point toward a minimum circularity of 0.59 ± 0.05 occurring between times 2.3 and 2.4.

The time evolutions of the center of mass and mean rise velocity of the bubble are shown in Figures 18(a) and (b), respectively. The center of mass moves similar to that of the first test case, reaching a slightly higher position of 1.138 at the end of the simulation (Table XIII). There are virtually no differences between the curves for the different grids. For the mean rise velocity, on the other hand, one can see that the curves corresponding to simulations computed on coarser grids differ quite much from the fine grid solutions but do converge toward them. Instead of the single

DOI: 10.1002/fld

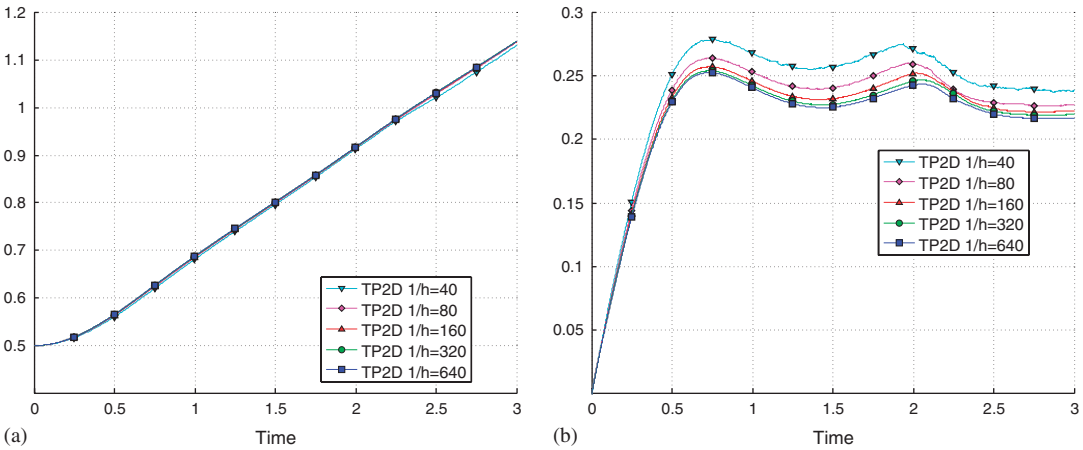

Figure 18. Center of mass and rise velocity for test case 2 and group 1 (TP2D): (a) center of mass and (b) rise velocity.

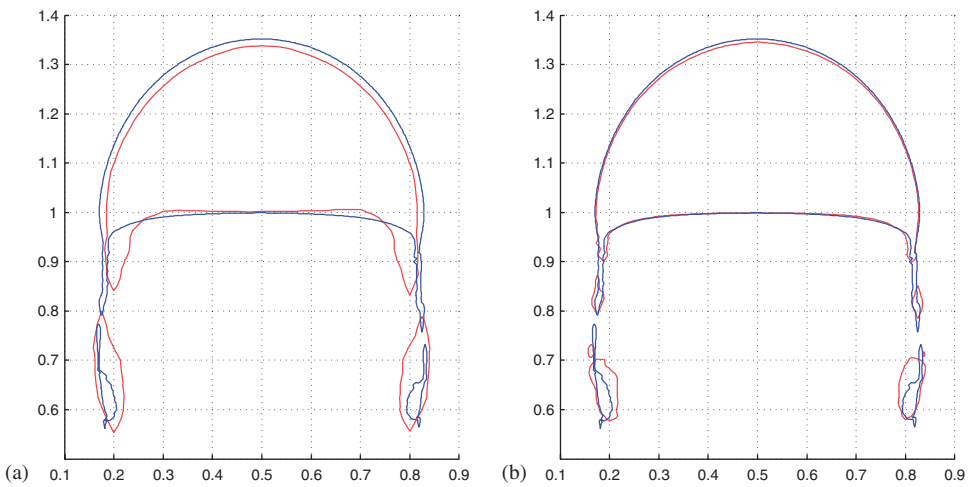

Figure 19. Test case 2 bubble shapes for the FreeLIFE code at time $t=3$. Coarse grid solutions (shown in red) compared with the shape computed on the finest grid $h=\frac{1}{160}$ (shown in blue): (a) $h=\frac{1}{40}$ and (b) $h=\frac{1}{80}$.

velocity maximum found in the first test case, there are now two, the first occurring at time 0.7332 with a magnitude of 0.2524 and the second one at $t=2.0705$ with a slightly smaller magnitude of 0.2434. Lastly note that in contrast to the circularity it is not possible to see when the break up occurs for these two benchmark quantities.

5.2. Group 2: FreeLIFE

The bubble shapes at the final time ($t=3$) computed with the FreeLIFE code on the three grid levels $h=1/[40, 80, 160]$ are presented in Figure 19. Although some sharp-edged filaments are

DOI: 10.1002/fld

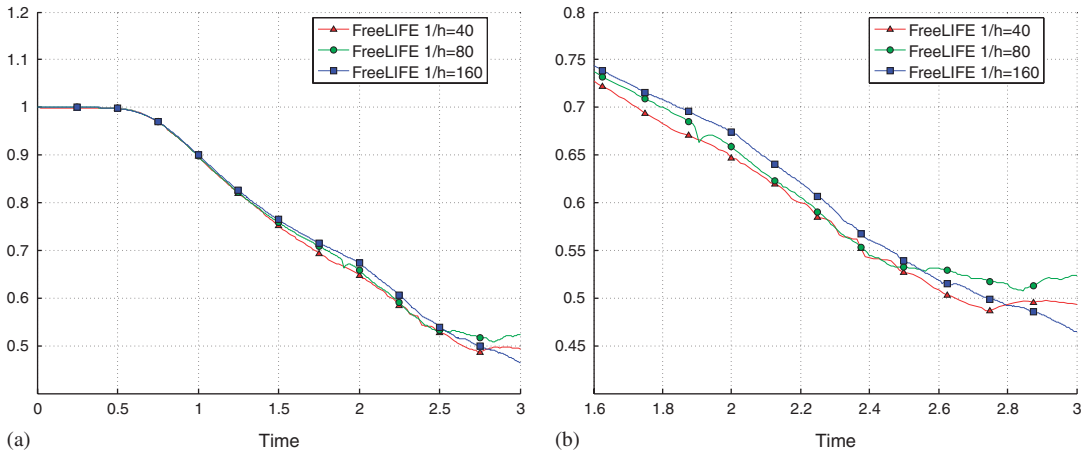

Figure 20. Circularity for test case 2 and group 2 (FreeLIFE): (a) circularity and (b) close-up of the circularity.

Table XIV. Minimum circularity and maximum rise velocities, with corresponding incidence times, and the final position of the center of mass for test case 2 and group 2 (FreeLIFE).

$1/h$	40	80	160
$\phi_{\min}$	0.4868	0.5071	0.4647
$t\|_{\phi=\phi_{\min}}$	2.7500	2.8438	3.0000
$V_{c,\max 1}$	0.2563	0.2518	0.2514
$t\|_{V_c=V_{c,\max 1}}$	0.7750	0.7188	0.7281
$V_{c,\max 2}$	0.2397	0.2384	0.2440
$t\|_{V_c=V_{c,\max 2}}$	1.9875	1.9062	1.9844
$y_c(t=3)$	1.0843	1.1099	1.1249

present despite refining the grids, the shapes do seem to converge toward the solution obtained on the finest grid. The main bulk of the bubble appears to be the easiest to capture correctly, showing only minor visible differences between the two finest grids (Figure 19(b)).

The curves for the circularity (Figures 20(a) and (b)) agree well and show a typical convergence behavior up to $t=1.8$ after which the bubble breaks up and no convergence trend can be seen anymore. Since the thin filaments do not retract after break up has occurred, there is no clear inflection point that could indicate the time of break up. The minimum circularity can thus be found toward the very end of the simulations, as can be seen in Table XIV.

The vertical position of the center of mass, shown in Figure 21(a), converges better than the circularity. The thin filaments apparently do not influence the overall movement too much since the curves are still approximately linear. A position of 1.1249 is reached by the bubble at the end of the simulation on the finest grid (Table XIV). A very good agreement can be seen for the curves describing the rise velocity up until the first maximum, occurring at $t=0.7281$ with a magnitude of 0.2514 on the finest grid (Figure 21(b) and Table XIV). From then on the curve corresponding to the simulation on the coarsest grid starts to show a somewhat irregular and oscillatory behavior. The other two curves corresponding to the finest grids keep in close contact until the second

DOI: 10.1002/fld

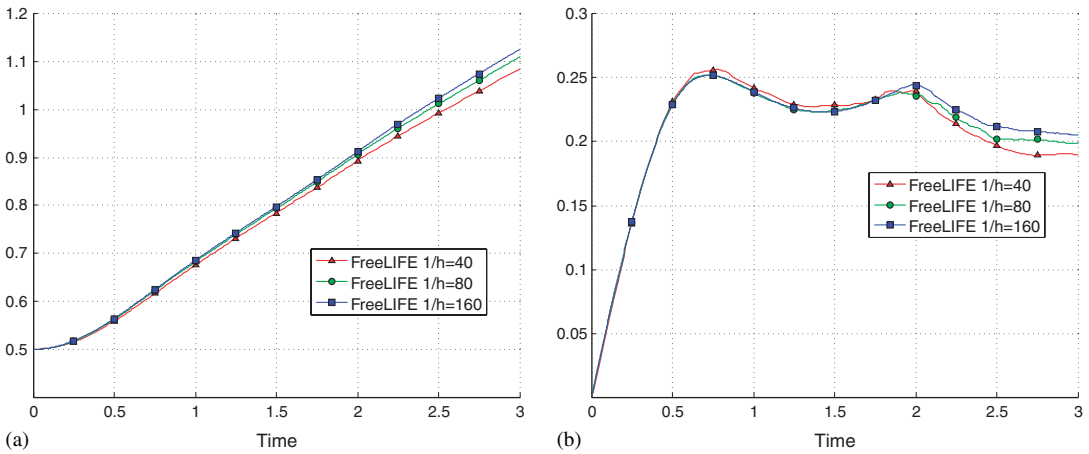

Figure 21. Center of mass and rise velocity for test case 2 and group 2 (FreeLIFE): (a) center of mass and (b) rise velocity.

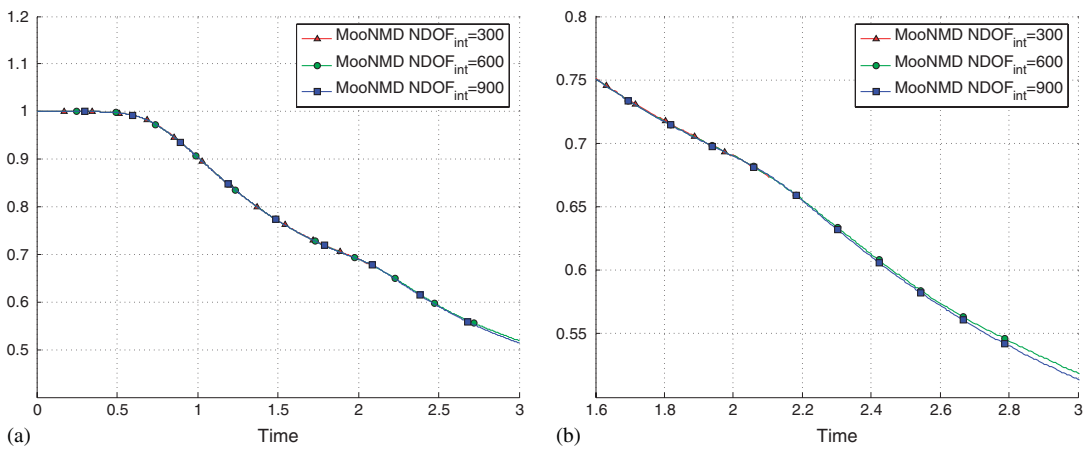

Figure 22. Circularity for test case 2 and group 3 (MooNMD): (a) circularity and (b) close-up of the circularity.

maximum, from where all curves show minor irregularities (most likely due to some oscillations in the velocity field close to the interface).

5.3. Group 3: MooNMD

For the third group (MooNMD), the results are as consistent as for the first test case with one exception, the simulation on the coarsest grid ($\text{NDOF}_{\text{int}} = 300$) failed at $t = 2.1$ due to the formation of very computationally unfavorable cell shapes in the thin filamentary regions. The Lagrangian approach used here could not treat break up automatically, and thus the bubble kept deforming more and more. This is evident from the curves for the circularity, which after the initial period decreases monotonically (Figures 22(a) and (b)).

DOI: 10.1002/fld

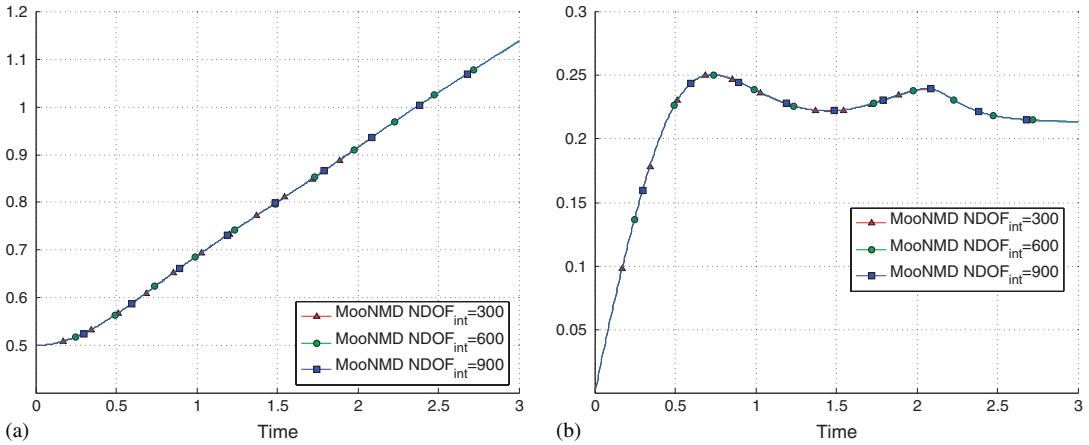

Figure 23. Center of mass and rise velocity for test case 2 and group 3 (MooNMD): (a) center of mass and (b) rise velocity.

Table XV. Minimum circularity and maximum rise velocities, with corresponding incidence times, and the final position of the center of mass for test case 2 and group 3 (MooNMD).

$\mathrm{NDOF}_{\mathrm{int}}$	300	600	900
$\phi_{\min}$	—	0.5191	0.5144
$t\|_{\phi=\phi_{\min}}$	—	3.0000	3.0000
$V_{c,\max 1}$	0.2503	0.2502	0.2502
$t\|_{V_c=V_{c,\max 1}}$	0.7317	0.7317	0.7317
$V_{c,\max 2}$	0.2390	0.2393	0.2393
$t\|_{V_c=V_{c,\max 2}}$	2.0650	2.0600	2.0600
$y_c(t=3)$	—	1.1380	1.1376

Figure 23(a) shows the linear time evolution of the center of mass. The curves agree completely irrespective of grid level, and from Table XV it is possible to see that the center of the bubble reaches a height of 1.1376 at the end of the simulation. Table XV also shows very consistent results for the two maxima found in the mean rise velocity. The first maximum occurred at $t=0.7317$ with a magnitude of 0.2502, while the second peak came later at $t=2.06$ with a velocity of 0.2393. These results are also perfectly mirrored by the plotted curves in Figure 23(b).

5.4. Overall results for test case 2

To compare the results for the second test case, a rising bubble with a significantly lower density compared to that of the surrounding fluid, the bubble shapes computed by the different codes are plotted against each other in Figure 24. It is evident that although all codes predict a similar shape for the main bulk of the bubble, there is no agreement with respect to the thin filamentary regions. The two first codes (TP2D and FreeLIFE) can handle break up automatically but do not, with the employed discretizations in space and time, agree what happens after. Since no criteria for the break up of the bubble have been implemented in the third code (MooNMD), the long thin trailing filaments remain intact.

DOI: 10.1002/fld

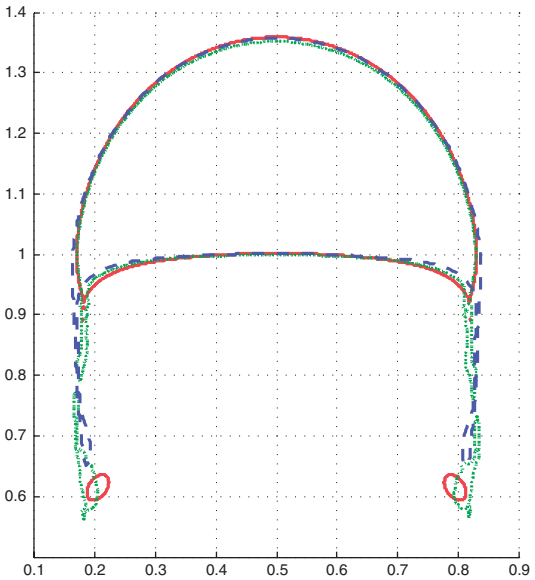

Figure 24. Bubble shapes at the final time ($t = 3$) for test case 2 (TP2D (solid red), FreeLIFE (dotted green), and MooNMD (dashed blue)).

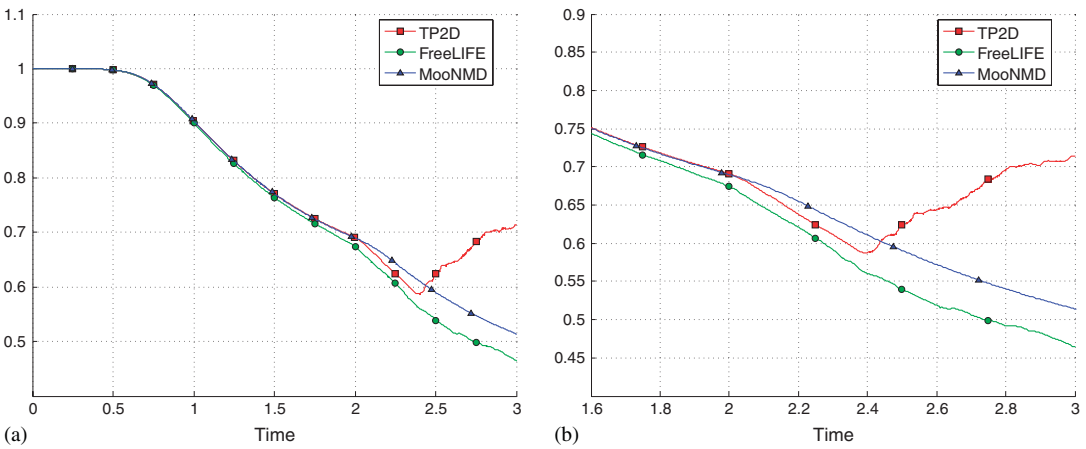

Figure 25. Circularity for test case 2 (all groups): (a) circularity and (b) close-up of the circularity.

The computed benchmark quantities for all groups agree very well with each other up until $t = 1.75$–2.0, which is quite notable considering the large viscosity and density ratios. The curves for the circularities (Figure 25(a)) coincide until about $t = 1.75$ after which significant differences start to appear. The main difference is that the circularity predicted by the TP2D code (group 1) starts to increase after the break up due to the retraction of the filaments (Figure 25(b)). Table XVI clearly shows that there is no real agreement between the codes concerning the minimum circularity.

DOI: 10.1002/fld

Table XVI. Minimum circularity and maximum rise velocities, with corresponding incidence times, and the final position of the center of mass for test case 2 (all groups).

Group	1	2	3
$\phi_{\min}$	0.5869	0.4647	0.5144
$t\|_{\phi=\phi_{\min}}$	2.4004	3.0000	3.0000
$V_{c,\max 1}$	0.2524	0.2514	0.2502
$t\|_{V_c=V_{c,\max 1}}$	0.7332	0.7281	0.7317
$V_{c,\max 2}$	0.2434	0.2440	0.2393
$t\|_{V_c=V_{c,\max 2}}$	2.0705	1.9844	2.0600
$y_c(t=3)$	1.1380	1.1249	1.1376

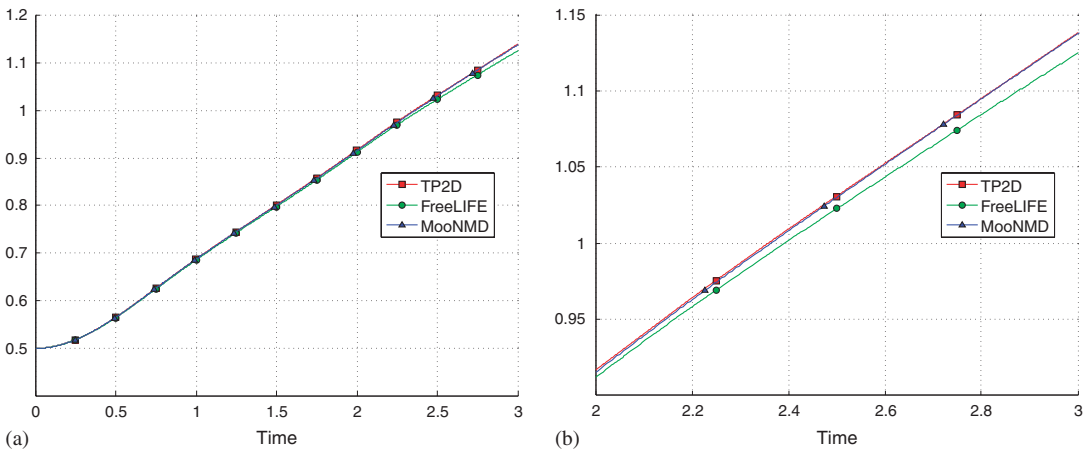

Figure 26. Center of mass for test case 2 (all groups): (a) center of mass and (b) close-up of the center of mass.

The vertical movement of the center of mass, shown in Figures 26(a) and (b), is predicted very similarly for all groups. Surprisingly in this case, the break up does not influence the overall averaged quantities to a significant degree. The estimated final position of the center of mass is 1.37 ± 0.01 (Table XVI). However, this value is quite meaningless since the final shape that the bubble most likely will assume is unknown.

Lastly the time evolution of the mean rise velocity is examined. Here, there is also a quite good agreement between the different codes. The first maximum is predicted to have a magnitude of 0.25 ± 0.01 and occur around $t = 0.73 \pm 0.02$ (Table XVI). The prediction of this maximum should be quite trustworthy since break up has not yet occurred and the curves are quite close to one another (Figure 27(a)). The second maximum is more ambiguous but should most likely have a somewhat smaller magnitude and occur around $t = 2.0$ (Figure 27(b)).

6. SUMMARY

Benchmark studies are valuable tools for the development of efficient numerical methods. A well-defined benchmark does not only assist with basic validation of new methods, algorithms, and

DOI: 10.1002/fld

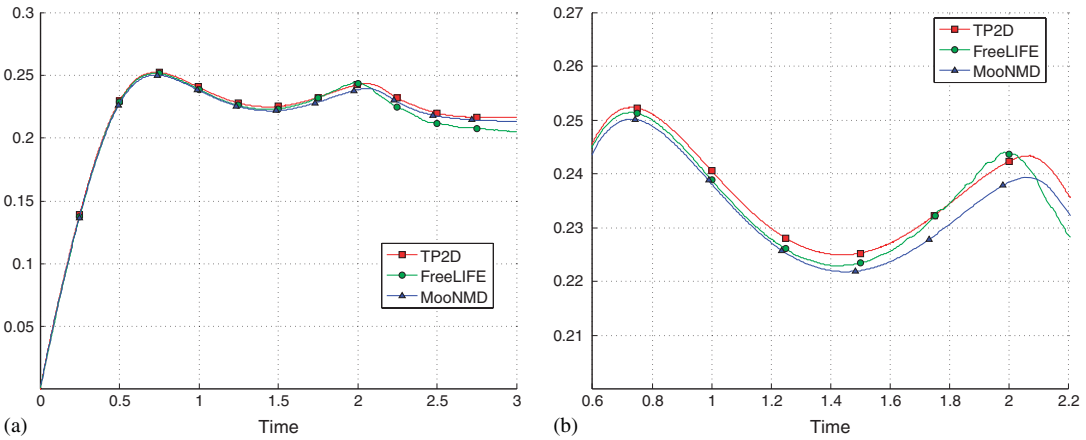

Figure 27. Rise velocity for test case 2 (all groups): (a) rise velocity and (b) close-up of the rise velocity.

software components, but can also help to answer more fundamental questions, such as '*How much numerical effort is required to attain a certain accuracy*?', which would allow for rigorous comparison of different methodologies and approaches.

Two benchmark test cases have been introduced and studied by conducting extensive computations. Both test cases concern the evolution of a single bubble rising in a liquid column while undergoing shape deformation. For the first test case, the deformation is quite moderate while the second bubble experiences significant topology change and eventually breaks up. In addition, a number of benchmark quantities have been defined, which allow for easier evaluation and comparison of the computed results since they can be used for strict validation in a 'picture norm' free form. They include the circularity and the center of mass, which both are topological measures, and also the mean rise velocity of the bubble. In future benchmarks it would be interesting to additionally track more complex quantities, such as force measures that involve derivatives of the dependent variables.

The studies showed that it was possible to obtain very close agreement between the codes for the first test case, a bubble undergoing moderate shape deformation, and thus establishing reference target ranges for the benchmark quantities. The second test case proved far more challenging. Although the obtained benchmark quantities were in the same ranges, they did not agree on the point of break up or even what the bubble should look like afterwards, rendering these results rather inconclusive. To establish reference benchmark solutions including break up and coalescence will clearly require much more intensive efforts by the research community. Other research groups are encouraged to join and participate in the benchmarks by contacting the authors. It is planned to collect all the submitted data and to provide a compilation of verified test configurations, in both two-dimensions and in the future also in three-dimensions, to allow for validation and evaluation of numerical simulation techniques for interfacial flow problems.

ACKNOWLEDGEMENTS

The authors like to thank the German Research foundation (DFG) for partially supporting the work under grants To143/9, Paketantrag PAK178 (Tu102/27-1, Ku1530/5-1), and Sonderforschungsbereich SFB708

DOI: 10.1002/fld

(TP B7) and SFB TR R30 (TPC3). The Swiss National Science Foundation is also acknowledged for supporting the work under Project No. 112166 'Finite element methods for Navier–Stokes equations with free-surface'.

REFERENCES

1. Annaland MS, Deen NG, Kuipers JAM. Numerical simulation of gas bubbles behaviour using a three-dimensional volume of fluid method. *Chemical Engineering Science* 2005; **60**(11):2999–3011. DOI: 10.1016/j.ces.2005.01.031.
2. Annaland MS, Dijkhuizen W, Deen NG, Kuipers JAM. Numerical simulation of behavior of gas bubbles using a 3-D front-tracking method. *AIChE Journal* 2006; **52**(1):99–110. DOI: 10.1002/aic.10607.
3. Bonometti T, Magnaudet J. An interface-capturing method for incompressible two-phase flows. Validation and application to bubble dynamics. *International Journal of Multiphase Flow* 2007; **33**(2):109–133. DOI: 10.1016/j.ijmultiphaseflow.2006.07.003.
4. Bothe D, Schmidtke M, Warnecke HJ. Direct numerical computation of the lift force acting on single bubbles. *6th International Conference on Multiphase Flow*, *ICMF2007*, Leipzig, Germany, 9–13 July 2007.
5. Chen L, Garimella SV, Reizes JA, Leonardi E. The development of a bubble rising in a viscous liquid. *Journal of Fluid Mechanics* 1999; **387**:61–96.
6. Esmaeeli A, Tryggvason G. Direct numerical simulations of bubbly flows. Part 1: low Reynolds number arrays. *Journal of Fluid Mechanics* 1998; **377**:313–345.
7. Hooper R, Cristini V, Lowengrub SSJS, Derby JJ, Macosko CW. Modeling multiphase flows using a novel 3D adaptive remeshing algorithm. In *Computational Methods in Multiphase Flow*, Brebbia CA, Power H (eds). Advances in Fluid Mechanics, vol. 29. Wessex Institute of Technology Press: U.K., 2001.
8. Koebe M, Bothe D, Warnecke HJ. Direct numerical simulation of air bubbles in water/glycerol mixtures: shapes and velocity fields. *FEDSM2003-45154 in Proceedings of the 2003 ASME Joint U.S.–European Fluids Engineering Conference*, Honolulu, U.S.A. ASME: New York, 2003.
9. Scardovelli1 R, Zaleski S. Direct numerical simulation of free-surface and interfacial flow. *Annual Review of Fluid Mechanics* 1999; **31**:567–603. DOI: 10.1146/annurev.fluid.31.1.567.
10. Unverdi SO, Tryggvason G. A front-tracking method for viscous, incompressible, multi-fluid flows. *Journal of Computational Physics* 1992; **100**(1):25–37. DOI: 10.1016/0021-9991(92)90307-K.
11. Ye T, Shyy W, Chung JN. A fixed-grid, sharp-interface method for bubble dynamics and phase change. *Journal of Computational Physics* 2001; **174**(2):781–815. DOI: 10.1006/jcph.2001.6938.
12. Christon AM, Gresho PM, Sutton SB. Computational predictability of time-dependent natural convection flows in enclosures (including a benchmark solution). *International Journal for Numerical Methods in Fluids* 2002; **40**(8):953–980. DOI: 10.1002/fld.395.
13. Hron J, Turek S. In *Proposal for Numerical Benchmarking of Fluid–Structure Interaction Between an Elastic Object and Laminar Incompressible Flow*, Bungartz H-J, Schäfer M (eds). Lecture Notes in Computational Science and Engineering, Fluid–Structure Interaction—Modelling, Simulation, Optimization, vol. 53. Springer: Berlin, 2006; 371–385. ISBN 3-540-34595-7.
14. John V, Matthies G. Higher-order finite element discretizations in a benchmark problem for incompressible flows. *International Journal for Numerical Methods in Fluids* 2001; **37**(8):885–903. DOI: 10.1002/fld.195.
15. Nabh G. On higher order methods for the stationary incompressible Navier–Stokes equations. *Ph.D. Thesis*, Universität Heidelberg, 1998. Preprint 42/98.
16. Turek S, Schäfer M. Benchmark computations of laminar flow around cylinder. *Flow Simulation with High-Performance Computers II* (*Notes on Numerical Fluid Mechanics*), vol. 52. Vieweg: Braunschweig, 1996; 547–566.
17. Turek S, Schäfer M, Rannacher R. Evaluation of a CFD benchmark for laminar flows. *Proceedings of ENUMATH*. World Science Publishing: Singapore, 1998.
18. Clift R, Grace JR, Weber ME. *Bubbles*, *Drops and Particles*. Academic Press: New York, 1978.
19. Bhaga D, Weber ME. Bubbles in viscous liquids: shapes, wakes and velocities. *Journal of Fluid Mechanics* 1981; **105**:61–85. DOI: 10.1017/S002211208100311X.
20. Martin J, Moyce W. An experimental study of the collapse of liquid columns on a rigid horizontal plane. *Philosophical Transactions of the Royal Society of London*, *Series A* 1952; **A 244**:312–324.
21. Bänsch E. Finite element discretization of the Navier–Stokes equations with a free capillary surface. *Numerische Mathematik* 2001; **88**(2):203–235. DOI: 10.1007/s002110000225.

22. Ganesan S. Finite element methods on moving meshes for free surface and interface flows. *Ph.D. Thesis*, Otto-von-Guericke-Universität, Fakultät für Mathematik, Magdeburg, 2006, published as book by docupoint Verlag Magdeburg (ISBN 3-939665-06-1).
23. Chen T, Minev PD, Nandakumar K. A projection scheme for incompressible multiphase flow using adaptive Eulerian grid. *International Journal for Numerical Methods in Fluids* 2001; **45**(1):1–19. DOI: 10.1002/fld.591.
24. Norman CE, Miksis MJ. Dynamics of a gas bubble rising in an inclined channel at finite Reynolds number. *Physics of Fluids* 2005; **17**(2):022102. DOI: 10.1063/1.1842220.
25. Sussman M, Puckett EG. A coupled level set and volume-of-fluid method for computing 3D and axisymmetric incompressible two-phase flows. *Journal of Computational Physics* 2000; **162**(2):301–337. DOI: 10.1006/jcph.2000.6537.
26. Wadell H. Sphericity and roundness of rock particles. *Journal of Geology* 1933; **41**:310–331.
27. Sussman M, Smereka P. Axisymmetric free boundary problems. *Journal of Fluid Mechanics* 1997; **341**:269–294.
28. Osher S, Sethian JA. Fronts propagating with curvature-dependent speed: algorithms based on Hamilton–Jacobi formulations. *Journal of Computational Physics* 1988; **79**(1):12–49. DOI: 10.1016/0021-9991(88)90002-2.
29. Turek S. *Efficient Solvers for Incompressible Flow Problems*, *An Algorithmic and Computational Approach*. Lecture Notes in Computational Science and Engineering, vol. 6. Springer: Berlin, 1999.
30. Hysing S, Turek S. The Eikonal equation: numerical efficiency vs algorithmic complexity on quadrilateral grids. *Proceedings of Algoritmy*, Slovak University of Bratislava, Bratislava, 2005; 22–31. ISBN 80-227-2192-1.
31. Kuzmin D, Turek S. High-resolution FEM–TVD schemes based on a fully multidimensional flux limiter. *Journal of Computational Physics* 2004; **198**(1):131–158. DOI: 10.1016/j.jcp.2004.01.015.
32. Hysing S. A new implicit surface tension implementation for interfacial flows. *International Journal for Numerical Methods in Fluids* 2006; **51**(6):659–672. DOI: 10.1002/fld.1147.
33. Hysing S. Numerical simulation of immiscible fluids with FEM level set techniques. *Ph.D. Thesis*, University of Dortmund, Institute of Applied Mathematics (LS III), Dortmund, 2007.
34. Turek S. On discrete projection methods for the incompressible Navier–Stokes equations: an algorithmical approach. *Computer Methods in Applied Mechanics and Engineering* 1997; **143**(3–4):271–288. DOI: 10.1016/S0045-7825(96)01155-3.
35. Parolini N. Computational fluid dynamics for naval engineering problems. *Ph.D. Thesis No. 3138*, École Polytechnique Fédérale de Lausanne (EPFL), 2004.
36. Parolini N, Burman E. A finite element level set method for viscous free-surface flows. *Applied and Industrial Mathematics in Italy*, *Proceedings of SIMAI 2004*. World Scientific: Singapore, 2005; 417–427.
37. Burman E, Parolini N. Subgrid edge stabilization for transport equations. *EPFL-IACS Report 09.2005*, 2005.
38. Burman E, Parolini N. A new reinitialization procedure for the finite element approximation of the level set equation. *EPFL-IACS Report 13.2005*, 2005.
39. Di Pietro DA, Lo Forte S, Parolini N. Mass preserving finite element implementations of the level set method. *Applied Numerical Mathematics* 2006; **56**(9):1179–1195. DOI: 10.1016/j.apnum.2006.03.003.
40. John V, Matthies G. MooNMD—a program package based on mapped finite element methods. *Computing and Visualization in Science* 2004; **6**(2–3):163–170. DOI: 10.1007/s00791-003-0120-1.
41. Girault V, Raviart PA. *Finite Element Methods for Navier–Stokes Equations*. Springer: Berlin, 1986.
42. Ganesan S, Matthies G, Tobiska L. On spurious velocities in incompressible flow problems with interfaces. *Computer Methods in Applied Mechanics and Engineering* 2007; **196**(7):1193–1202. DOI: 10.1016/j.cma.2006.08.018.
43. Dziuk G. An algorithm for evolutionary surfaces. *Numerische Mathematik* 1991; **58**:603–611.
44. Ruschak KJ. A method for incorporating free boundaries with surface tension in finite element fluid-flow simulators. *International Journal for Numerical Methods in Engineering* 1980; **15**(5):639–648. DOI: 10.1002/nme.1620150502.
45. Rannacher R. Incompressible viscous flows. *Encyclopedia of Computational Mechanics*, vol. 3. Wiley: New York, 2004; 155–182.
46. Shewchuk JR. Triangle: engineering a 2D quality mesh generator and Delaunay triangulator. *Applied Computational Geometry*: *Towards Geometric Engineering*. Lecture Notes in Computer Science, vol. 1148. Springer: Berlin, 1996; 203–222.